Kinematics and Statics of Eccentric Soft Bending Actuators with External Payloads

Chenghao Yang [a], Rongjie Kang [a,*], David T Branson [b], Lisha Chen [c], Jian S Dai [d]
[a] Key Laboratory of Mechanism Theory and Equipment Design of the Ministry of Education, Centre for Advanced Mechanisms and Robotics, Tianjin University, China
[b] Faculty of Engineering, University of Nottingham, U.K.
[c] School of Mechanical Engineering, Tianjin Polytechnic University, China
[d] Centre for Robotics Research, King's College London, U.K.

Abstract
Soft bending actuators, born with the considerable capacity of structural flexibility and environmental adaptability, have been widely favored for years. However, the highly nonlinear coupling between force and deformation in such robots are very complex, especially considering the external payloads. This paper puts forward a concept of eccentric soft bending actuators (ESBAs) that can exhibit different output characteristics by modifying the geometric parameters. A virtual trajectory based kinematic model is introduced to describe the deformation of ESBAs so that the screw theory based product of exponentials (POE) formula is applied to the analysis of such soft tentacle-like structures for the first time. Following this, the static model takes the input pressure, external payloads, and material parameters into account by utilizing the principle of minimum potential energy, making a generalized mathematical expression. The proposed model is then verified via finite element methods (FEM), and finally through experiments. An application example shows that the Particle Swarm Optimization (PSO) is introduced to find appropriate geometric parameters to make an ESBA have maximum stiffness.
Keywords:
Eccentric soft bending actuators; Screw theory; Statics model; Parameters optimization;

1. Introduction

Soft robots have demonstrated excellent advantages in terms of human-machine interaction, unstructured environment exploration, and bionic systems [1]. Composing of materials with Young's modulus in the order of 10^4–10^9Pa, they possess softness, body compliance, shape sensing, and power storage features [2, 3]. There are basically two types of materials used for them: 1) Smart materials, including shape memory alloy (SMA), ionic polymer metal composite (IPMC), dielectric elastomers (DE) and responsive hydrogels, that can deform themselves under activation of physical fields or in specific chemical environments [4-8]; 2) Traditional elastic materials, such as rubbers, plastics, and Ni-Ti alloys, that require additional fluid or cable mechanisms to exert actuating forces on their structures [9-11].

Powered by pneumatic pressure, soft bending actuators are always made of rubbers, which are able to bend their body with high power to weight ratio and makes it widely developed in previous works. Whitesides et al [12] used a series of pneumatic networks (PneuNet) of channels embedded in elastomers that inflate like balloons for actuation. In later work, Whitesides et al [13] proposed a new design for PneuNet reducing the amount of gas needed for inflation, and thus increased its speed of actuation. Elsayed et al [14] introduced a pneumatically actuated silicone module with three cylindrical chambers for robotic surgery application, which can almost bend in any direction.

Shepherd et al [15] proposed the foam based soft bending and extension actuators that have an interconnected open-pore network and require no additional molded air channels. Paik et al [16] introduced a vacuum-powered soft pneumatic actuator to achieve multimodal locomotion, object manipulation, and stiffness tuning by using just a single, shared vacuum power. Fiber-Reinforced actuators are another kind of soft pneumatic actuators. Wood et al [17] presented a semicircular elastomeric actuator with an air chamber, an inextensible layer at the base and fibers winding along the length of the actuator, which can change bending radius by varying the fibers angle. McKibben pneumatic muscles, primarily designed to contract and extend in the axial direction, can also achieve bending movement if multiple muscles are arranged in parallel [18, 19]. In summary, the actuation principle of the soft bending actuators is basically similar, and the fluid is used to expand the air chamber, causing the extension of the soft material around it. At the same time, the inextensible material is added on the other side or the stiffness of the part of the material is higher so that the elongation of the soft actuators in the axial direction is different, and the bending phenomenon occurs.

In the field of robotics, it is essential to understand the mechanical characteristics of the actuators, including their displacement and output force [20]. For the soft bending actuators, their deformations and force conditions often affect and restrict each other. Building an experimental platform is perhaps the most accurate and objective method to observe the coupled behaviors of such actuators. Sun et al [21] used experiments to obtain the outputs of soft actuators by developing two measurement platforms and then gave a simple model to provide physical insight into the observed behaviors. Similarly, Wereley [22] et al presented a static model of McKibben artificial muscles by experimentally characterizing their behavior with basic geometric parameters. However, it can only be targeted at the soft actuators that have already been made, but difficult to predict new ones during a design process. Finite Element Method (FEM) is a feasible simulation and forecasting tool for soft actuators. Moseley et al developed a FEM based method to simulate the displacement and blocked-force performance for a soft pneumatic actuator. Such methods can be extended to a diverse range of soft materials and design parameters [23]. However, the FEM based approaches are difficult to reveal the intrinsic characteristics of soft actuators and hard to find inverse solutions.

On the other hand, analytical models have been used as an effective way to estimate the deformation and output forces. The pseudo-rigid-body approach was first proposed by Howell [24]. The deformation of flexible structures can be discretized to many short-length links hinged by torsion springs, so that classical methods for a rigid body can be used for analysis. Satheeshbabu and Krishnan [25] used a modified pseudo-rigid-body model to captures the axial and bending stiffnesses of contracting fiber reinforced elastomeric enclosures. Venkiteswaran and Su [26] presented a three-spring based pseudo-rigid-body model for short beams to calculate the deflection of a soft joint made of elastomer material. However, it may introduce deviation by using virtual links to fit a continuous curve, especially when analyzing large bending deformation of the slender structures. Then the constant curvature based approach was proposed to describe the deformation of continuum robots by establishing the mappings between the configuration space and task space [27]. Nevertheless, it is very complicated since a large number of coordinate frames need to be built on each segment of the robot to fit the deformation by using the homogeneous coordinates transformation [28, 29]. Screw theory is the algebra of vectors, such as forces and velocity, that arises in the kinematics and dynamics of rigid bodies [30]. It was extended for revisiting the classic theory of Timoshenko beams by Selig and Ding [31] in 2009. Then Ding and Dai [32] proposed a screw theory and Lie Groups based method to investigate the deflection problems in

serial and parallel mechanisms with compliant links. Qi et al [33] used a framework of a screw theory including a twist deflection, a wrench, and the compliance matrix to establish the analytic model of a continuum robot. The same framework was also published in [34] combining the Euler-Bernoulli Beam theory to analyze a multi-backbone continuum robot. However, all the above methods assumed that the deformation of the bending structures is small, and the statics is solved by introducing a compliance matrix that is difficult to express in the case of soft actuators. There were also many other models of the rod-driven continuum robots with backbones [35, 36]. In [37], the principle of the virtual power was utilized for dynamics of the multi-backbone continuum. But it is not suitable for the fully soft actuators made of silicone rubber. Trivedi et al [38] presented a geometrically exact model for soft manipulator that incorporates the effects of material nonlinearities, distributed weight and payload. However, considering a soft bending actuator as a beam model is not efficient to characterize its internal geometric relationship if the structure of the actuator is not symmetric. Munro et al [10] presented a static model for pneumatic muscles that considered the mechanical and the geometric properties. Bishop-Moser et al [39] analyzed the statics of fiber-reinforced pneumatic actuators that consider the fiber angles to obtain the rotation deformation when pressurized. But both two models are one-dimensional which is not suitable for the bending actuators usually working in a two-dimensional sagittal plane. Polygerinos et al [40] proposed a quasi-static analytical model for soft fiber-reinforced bending actuators based on Newtonian mechanics and have been implemented in bending control. Trivedi et al [41] developed optimal designs for soft robotic manipulators, OctArm, involving the Cosserat rod theory and the genetic algorithm-based optimizer to maximize the load capacity of the arm. Walsh et al [42] presented a nonlinear elasticity based analytical model of the fiber-reinforced soft actuators with an optimization to identify the design parameters for actuators that follow a certain trajectory upon pressurization. However, previous models assume actuators have constant curvature or consider the output displacement by ignoring external forces, which leads to an incomplete analysis of performance.

In this paper, we put forward a concept of eccentric soft bending actuators (ESBAs). It can be seen as a generalized case of the conventional fiber-reinforced soft bending actuators so that a generalized model can be introduced. A concise but effective kinematic model is developed by involving the trajectory of a virtual rigid manipulator and the screw theory based POE formula is applied to the analysis of such soft actuators for the first time. Regarding the statics, the pressure input and external payloads are taken into account by utilizing the principle of minimum potential energy instead of previously reported Newtonian mechanics. Different from measuring the blocked-force on a fixed point, we focus on the stiffness index to describe the large and nonlinear displacement coupled with the payload in ESBAs.

The arrangement of this paper is as follows: Section 2 introduces the concept of the ESBAs. Section 3 gives a detailed analysis for proposed ESBAs including the kinematics and statics. Section 4 describes how the FEM model and experimental platform are developed, and then the proposed analytical model is validated by sets of simulation and experimental results. Section 5 gives a further case study about how to design an ESBA with maximal stiffness to explain the effectiveness of the above model. In Section 6, the conclusions and outlooks are presented.

2. Concept of ESBAs

Like classical soft bending actuators, ESBAs also rely on the chamber and the inextensible layer to generate different expansion rates at different layers in the axial

direction when producing a bending operation under pressure. It is a more generalized situation of conventional cylindrical fiber-reinforced soft actuators because the geometric parameters of the chamber can be modified, whose analytic model becomes a generalized approach for this type of actuators. The fabrication process of these actuators is shown in Figure 1. The ESBA used in this study is composed of silicone rubber curing in a 3D-printed mold whose length and external radius are marked as L and r_1, respectively. The position and radius of the inserted Plexiglas bar determine the eccentric distance d and the radius r_2 of the chamber, respectively. Then, a nylon fiber mesh is implanted close to the bottom as an inextensible layer. To avoid the rubber expanding in the radial direction, Kevlar fibers are double helix winded.
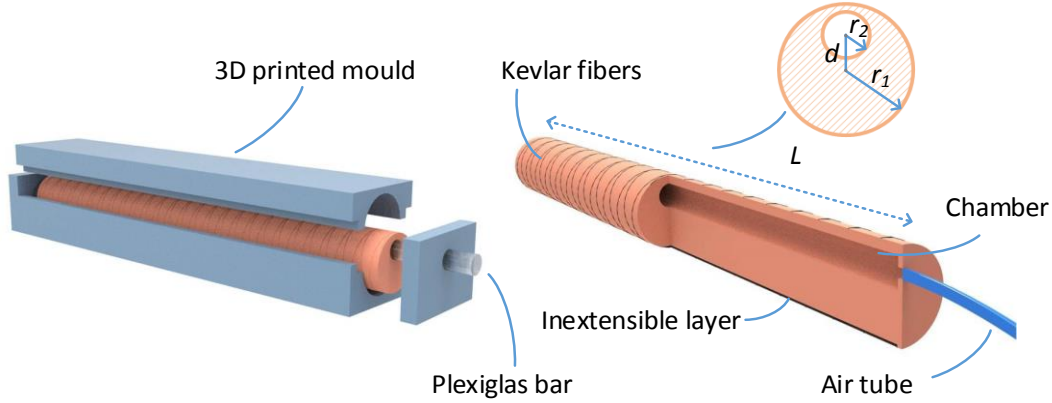

Figure 1. Fabrication and specification of the soft actuator

By proposing the above concept of ESBAs, researchers have more freedom to design the resulting deformation and stiffness of actuators, through the implementation of different combinations of the eccentric distance d and the radius of the chamber r_2. Therefore, the characters of ESBAs become more complicated and less intuitive. For instance, if we require maximum stiffness at a desired bending position of the ESBA, we must make the moment generated by air pressure as large as possible. Generally, with the greater air pressure input P, the farther eccentric distance d and the larger radius of chamber r_2, the greater moment the actuator will generate on each cross section. However, all these variables will jointly affect the actual bending position of the ESBA leading the bending angle larger. Then the question becomes how to determine the values of these three variables to make a trade-off between stiffness and position. This curiosity drove us to carry out a generalized modeling analysis that can describe all of these factors.

3. Modeling of the ESBA
3.1 Kinematics
In the previous works [27], it is necessary to establish a large number of local coordinate systems on the flexible body to solve the kinematics of such bending structures. On the other hand, the POE formula, which is based on the screw theory and essentially based on the characteristics of rigid body motion, can use only two coordinate frames, the base frame S and the tool frame T, to solve the kinematics using a more concise expression. These make POE formula a superior alternative to the Denavit-Hartenberg method in rigid-body robots [43-45].

This section will introduce a method for representing the deformation curve of ESBAs by motion trajectory of a virtual rigid robot in the sagittal plane. The trajectory generated by the endpoint of the series rotating joint robot is a combination of multiple tangentially connected arcs in the sagittal plane perpendicular to the joint axis. This

method has a concise form to build the kinematics of soft actuators according to the following steps:
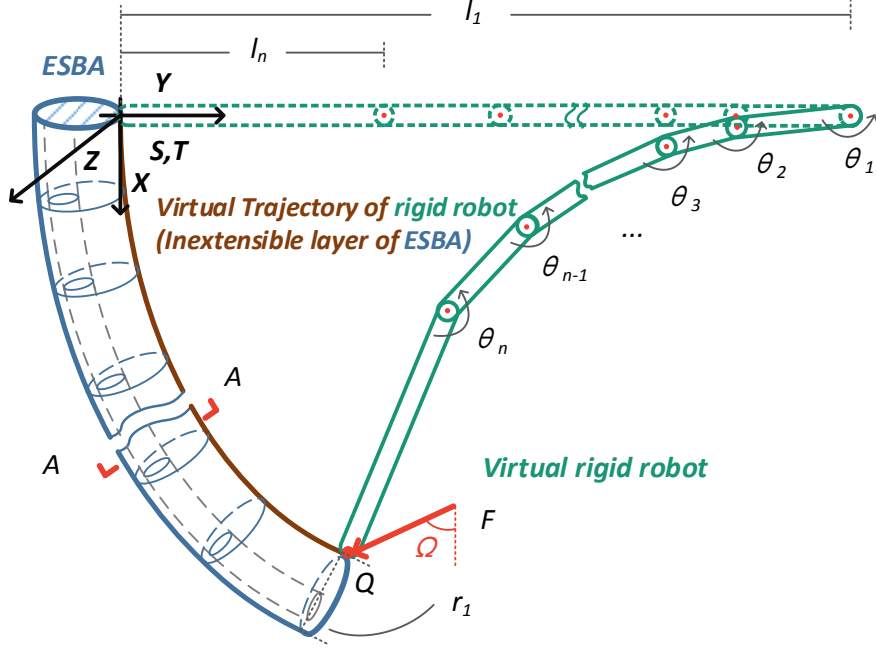

Figure 2. A typical case of the ESBA under external force

a) Assume a typical case of the ESBA when under the external payload applied at the endpoint, Q, in the horizontal direction, and divide the ESBA into n equal segments as shown in Figure 2. The inextensible layer of the ESBA within the sagittal plane, the brown line, is on the ventral side whose length is L.

b) In the sagittal plane, set the base frame S at the starting point of the inextensible layer. The x-axis is parallel to the tangential direction of the inextensible layer, and the direction is vertically downward. The y-axis is perpendicular to the tangential direction of the inextensible layer, and the direction is horizontal to the right.

c) Imagine there is a virtual rigid robot possessing n revolute joints whose rotation angles are $\boldsymbol{\theta}=[\theta_1, \theta_2, \ldots, \theta_n]$ about the z-axis, as shown in Figure 2. Its initial configuration ($\boldsymbol{\theta}=0$) lies along the y-axis with the endpoint located at the origin of the base frame S, depicted by the green dashed line. The length of the ith link is unknown but the distance from the ith joint to the origin of the base frame S is represented by l_i. Note that, l_i and θ_i are also the bending radius and bending angle of each segment of the ESBA, respectively. Thus, the geometric relationship between the rotation angle θ_i, joint distance l_i and trajectory length of the virtual rigid robot (i.e. the length of the actuator L) can be derived as

$$\frac{L}{n} = l_i \theta_i, \quad (i = 1, 2, ..., n) \tag{1}$$

d) Set the tool frame T at the end of the virtual rigid robot. The transformation between tool and base frames at $\boldsymbol{\theta}=0$ is given by a unit matrix $g_{\text{st}}(0)=\boldsymbol{I}$. The screw motion of each joint is written according to the screw theory. Note that

$$\omega_1 = \omega_2 = \omega_3 = \cdots = \omega_n = \begin{bmatrix} 0 \\ 0 \\ 1 \end{bmatrix} \in \mathbb{R}^3$$

are unit vectors in the direction of the twists. Then we choose any point $q_i \in \mathbb{R}^3$ on the joint axis ($i=1,2,\ldots,n$)

$$q_1 = \begin{bmatrix} 0 \\ l_1 \\ 0 \end{bmatrix} \quad q_2 = \begin{bmatrix} 0 \\ l_2 \\ 0 \end{bmatrix} \quad q_3 = \begin{bmatrix} 0 \\ l_3 \\ 0 \end{bmatrix} \quad \cdots \quad q_n = \begin{bmatrix} 0 \\ l_n \\ 0 \end{bmatrix}$$

This yields twists

$$\xi_1 = \begin{bmatrix} l_1 & 0 & 0 & 0 & 0 & 1 \end{bmatrix}^{\mathrm{T}}$$

$$\xi_2 = \begin{bmatrix} l_2 & 0 & 0 & 0 & 0 & 1 \end{bmatrix}^{\mathrm{T}}$$

$$\xi_3 = \begin{bmatrix} l_3 & 0 & 0 & 0 & 0 & 1 \end{bmatrix}^{\mathrm{T}}$$

$$\vdots$$

$$\xi_n = \begin{bmatrix} l_n & 0 & 0 & 0 & 0 & 1 \end{bmatrix}^{\mathrm{T}}$$

The vector ξ_n can be converted into homogeneous coordinate of a 4×4 matrix $\hat{\xi}_n$ by the hat operator [44], and the details are shown in Appendix (a). Combining the individual joint motions, the kinematics map $\boldsymbol{g}_{\mathrm{st}}$:Q→SE(3), is given by the POE formula

$$\boldsymbol{g}_{st}(\boldsymbol{\theta}) = e^{\hat{\xi}_1 \theta_1} e^{\hat{\xi}_2 \theta_2} e^{\hat{\xi}_3 \theta_3} \cdots e^{\hat{\xi}_n \theta_n} \boldsymbol{g}_{st}(0) = \begin{bmatrix} \boldsymbol{R} & \boldsymbol{P} \\ 0 & 1 \end{bmatrix} \tag{2}$$

where $\boldsymbol{R}$ and $\boldsymbol{P}=[x;y;0]$ are the orientation and the end position of the ESBA.

The number of n depending on the complexity of the deformation and required accuracy. Increasing the number of n results in a higher resolution of the analytical model owing to a higher number of segments to describe the deformation and vice versa.

3.2 Statics

The banding angle θ of the ESBA is coupled with the forces such as air pressure, restraining force of fiber and external payload. To establish the static model, in this section, the principle of minimum potential energy is used since there is no need for establishing Newtonian equilibrium equations in every segment [46]. Note that this part of analysis returns to ESBA itself, not the virtual rigid robot. The total potential energy is expressed as

$$U = -P\Delta V + U_{\mathrm{a}} + U_{\mathrm{r}} + U_{\mathrm{f}} \tag{3}$$

where P is the air pressure, and ΔV is the volume change of the chamber. U_{a}, U_{r}, and U_{f} are the potential energy of the rubber in the axial, radial direction and the potential energy of external forces, respectively [47]. Then we obtain $\boldsymbol{\theta}=[\theta_1;\theta_2; \theta_3;\ldots, \theta_n]$ by taking the derivative of the function U and setting it equal to zero, which means the total potential energy is minimum in this state:

$$\frac{\partial U}{\partial \theta_1} \mathrm{d}\theta_1 + \frac{\partial U}{\partial \theta_2} \mathrm{d}\theta_2 + \cdots \frac{\partial U}{\partial \theta_{n-1}} \mathrm{d}\theta_{n-1} + \frac{\partial U}{\partial \theta_n} \mathrm{d}\theta_n = 0 \tag{4}$$

The calculation of each term will be explained as follows.

3.2.1 The potential energy of the compressed air

Poisson's ratio of silicone rubber is close to 0.5, so it is usually assumed to be incompressible [48]. Therefore, when the ESBA bends, each segment's volume change is mainly due to the volume change of the air chamber under pressure. Thus, the potential energy of the compressed air in Equation (3) is expressed as

$$-P\Delta V = -P\left[\sum_{i=1}^{n} \pi r_1^2 (R_i + r_1)\theta_i - \pi r_1^2 L\right] = -Pr_1^3 \pi \sum_{i=1}^{n} \theta_i \tag{5}$$

3.2.2 The potential energy of the rubber

Silicone rubber is a hyperelastic and nonlinear material, previously described by Neo-Hookean, Yeoh, Mooney-Rivlin, and Ogden constitutive models [49]. However, when the strain is in the range of 0–1, the stress almost increases linearly so Young's modulus E is still suitable for analyzing the soft actuators [13, 14, 50].

When the ESBA bends, the potential energy of the rubber in the axial direction U_a can be calculated by subtracting the potential energy of the part occupied by the air chamber from the potential energy of the solid cylinder. In Figure 3(a), the area of the shaded region is $dS_{sld}=2r_1^2\sin^2\alpha d\alpha$ and the detail is shown in Appendix (b). For the ith segment, the elongation in the axial direction of the shaded region on the solid cylinder is $\lambda_{sld}=r_1(1-\cos\alpha)\theta_i$. The potential energy of the shaded region on the solid cylinder in the axial direction is

$$d\psi_{sld} = \frac{nE\lambda_{sld}^2}{2L}dS_{sld} \tag{6}$$

Similar, the area of the shaded region on the air chamber is $dS_{cmb}=2r_2^2\sin^2\beta d\beta$. For the ith segment, the elongation in the axial direction on the air chamber is $\lambda_{cmb}=(r_1+d-r_2\cos\beta)\theta_i$. The potential energy of the shaded region on the air chamber in the axial direction is

$$d\psi_{cmb} = \frac{nE\lambda_{cmb}^2}{2L}dS_{cmb} \tag{7}$$

Thus, the potential energy of the rubber in the axial direction U_a can be expressed as:

$$U_a = \sum_{i=1}^{n}(\int_0^\pi d\psi_{sld} - \int_0^\pi d\psi_{cmb}) = \sum_{i=1}^{n}\theta^2_i nE\pi\frac{5r_1^4 - 4r_2^2(r_1+d)^2 - r_2^4}{8L} \tag{8}$$
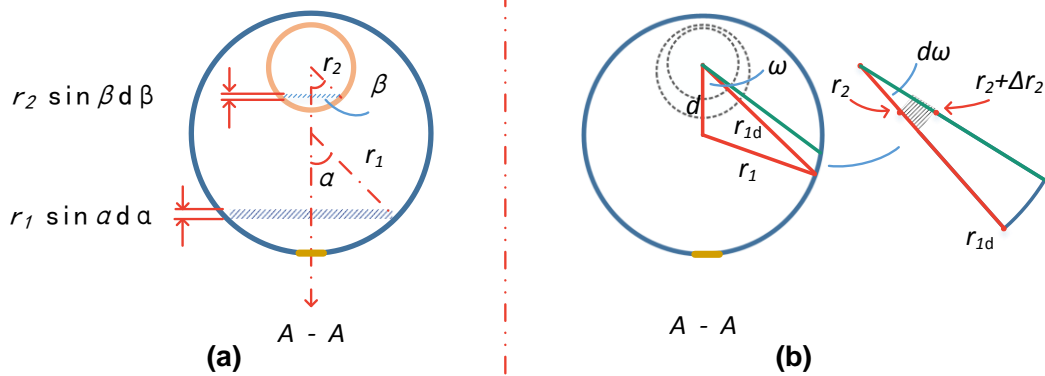

Figure 3. The cross-section of inflating chamber

For elastic potential in the radial direction, we assume that the cross sections of the chamber as shown in Figure 3(b) are always circles whose radii are $r_2+\Delta r_{2i}$ after expanding and ignore the small impact of this assumption on the eccentric distance d. This is reasonable because the outer surface of the ESBA has fiber constraints that limit radial expansion. As the volume of the rubber is invariable, the volume of the rubber before and after deformation can be presented as

$$\pi\frac{L}{n}(r_1^2 - r_2^2) = \pi r_1^2(\frac{L}{n}+r_1\theta_i) - \pi(r_2+\Delta r_{2i})^2(\frac{L}{n}+r_1\theta_i+d\theta_i) \tag{9}$$

Then the radii change of the chamber can be derived as

$$\Delta r_{2i} = \sqrt{\frac{Lr_2^2 + nr_1^3\theta_i}{L+nd\theta_i+nr_1\theta_i}} - r_2 \tag{10}$$

This results in a discontinuous distribution of wall thickness, but since r_2 is small, and as the number of segments increases, the steps of adjacent segments can be ignored. Along the radial direction of the chamber the rubber has the same stress P, so here we assume the strain in the radial direction is also the same because of the same Young's modulus. Therefore a special case in the sagittal plane can be presented as $\varepsilon = \Delta r_{2i}/(r_1 - r_2)$. In the red triangle in Figure 3(b), ω is an internal angle between edge d and edge r_{1d}, and then r_{1d} can be derived by using cosine law, where

$$r_{1d} = \sqrt{r_1^2 - d^2 \sin^2 \omega} + d \cdot \cos \omega \tag{11}$$

is the only positive solution as $r_1 > d$. In every sector of the ith segment, the approximate average area under pressurized air is

$$dS_{sctr} = \frac{r_{1d} + r_2}{2} \left(\frac{L}{n} + r_1 \theta_i\right) d\omega \tag{12}$$

and the initial length in the radial direction is $r_{intl} = r_{1d} - r_2$. The potential energy in the radial direction of the rubber is then calculated by integrating every sector's potential energy in each segment and adding them all:

$$U_r = \sum_{i=1}^{n} \int_0^{2\pi} \frac{E r_{intl} \varepsilon^2}{2} dS_{sctr} = \sum_{i=1}^{n} \frac{E\pi(L + r_1\theta_i)(r_1 + r_2)}{2n(r_1 - r_2)} \left(\sqrt{\frac{Lr_2^2 + nr_1^3\theta_i}{L + nd\theta_i + nr_1\theta_i}} - r_2\right)^2 \tag{13}$$

3.2.3 The potential energy of external forces

The external forces also generate potential energy to the system including external payloads, gravity, and restraints in the radial direction initiated by the Kevlar fibers [47]. In this model, the payload is applied to the endpoint of the ESBA at an angle of Ω with respect to the vertical direction as shown in Figure 2, therefore this part of the potential energy is

$$\psi_{pyl} = yF \sin \Omega + (l - x)F \cos \Omega \tag{14}$$

We then consider that the center of gravity is located at the geometric center of every segment, and their coordinates (x_i, y_i) can be calculated by replacing θ_n in Equation (2) with $\theta_i/2$. The potential energy caused by gravity is

$$\psi_{grvty} = \frac{MgL}{2} - \frac{Mg}{n} \sum_{i=1}^{n} x_i \tag{15}$$

Reinforced fibers do negative work on the ESBA, but only in the axial direction. The tension η in the fibers follows their winding direction, which can be decomposed as shown in Figure 4.
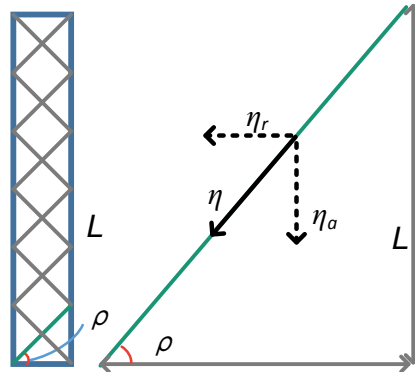

Figure 4. The fiber of ESBA and its force condition

Note that, we do not care about the potential energy in fibers which is very small, but we consider its restraining force as one of the external forces. In this way, the restraining

force of fibers in the radial direction balance the radial expansion force from the chamber which is

$$2N\eta_r = 2\pi r_2 (L + r_1\theta_{TOL})P \tag{16}$$

where

$$\theta_{TOL} = \sum_{i=1}^{n} \theta_i \tag{17}$$

presents the total bending angle. $N=(L+r_1\theta_{TOL})/(2\pi r_1\tan\rho)$ indicates the number of turns per fiber. Through this, restraining force in the axial direction is derived as $2\eta_a = 2\eta_r \tan\rho$, and the displacement in the axis direction is approximate to $r_1\theta_{TOL}$, whose product indicates the external potential energy generated by the fibers shown as:

$$\psi_{fbrs} = 4P\pi^2 r_1^2 r_2 \theta_{TOL} \tan^2\rho \tag{18}$$

The potential energy of external forces is then shown as:

$$U_f = \psi_{pyl} + \psi_{grvty} + \psi_{fbrs} \tag{19}$$

4. FEM and Experimental Validations
4.1 The prototype

We choose the Silicone rubber (Elastosil M4601, Wacker Chemie AG) to build the prototype according to the method mentioned in Section 2 and the parameters of the ESBA are summarized in Table 1. Note that the mass of the prototype is just 35g. Moreover, the total length of the ESBA is also relatively short, thus, the analysis in the following will ignore the influence of gravity.

Table 1 Parameters for the proposed ESBA

Description	Symbol	Value
Initial length	L	135mm
External radius	r_1	8mm
The radius of the chamber	r_2	3mm
Eccentric distance	d	4mm
Angle of fibers	ρ	10°
Mass	M	35g

4.2 The FEM setup

The commercial FEM software Abaqus/CAE (SIMULIA, Dassault Systèmes) is used to evaluate the proposed analytical model and prototype of ESBA under various pressures and external forces to validate them in the simulation.

The elastomeric samples were tested by uniaxial tensile experiment, ignoring the nonlinearity of the material as mentioned in Section 3.2.2 [13], and Young's modulus of E=0.54MPa was obtained by the linear fitting. In addition, Young's modulus of the Kevlar fiber and inextensible layer was assigned to 31067MPa and 6500MPa with Poisson's ratio of 0.36 and 0.2 based on material properties, respectively [40]. We imported a simplified 3-D model, built in SolidWorks (SolidWorks, Dassault Systèmes), to reduce the time of calculation by ignoring minor details such as the grooves at the outer face. The winding fibers were generated by an open source code [40]. The silicone rubber and fibers were modeled using solid tetrahedral quadratic hybrid elements (Abaqus element type C3D10H) and quadratic beam elements (Abaqus element type B32), respectively. After defining boundary conditions that we fixed the ESBA at one end, the pressure was applied to all the internal walls of the chamber and the payload was exerted at the other end in the horizontal direction. Here, we present one of the

FEM results, whose corresponding design parameters and input pressure are also shown in Figure 5. The bending angle of the ESBA under these parameters is 259.5° with a constant radius of curvature as there is no payload added. However, if there are external payloads, it will clearly bend with a non-constant radius of curvature as can be seen in Section 4.4.2. Later, we will continue to carry on a detailed analysis of this characteristic.
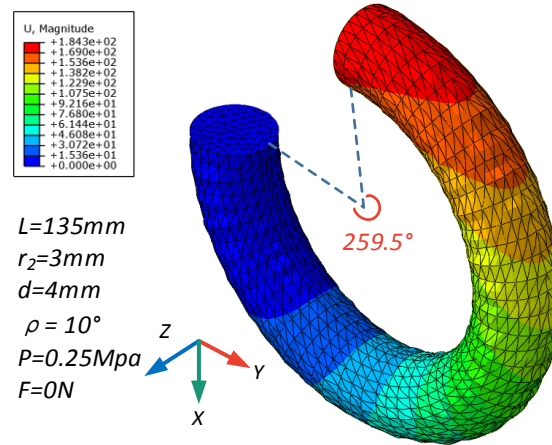

Figure 5. A FEM result without payloads

4.3 The experimental platform

To validate the analytical and FEM models, an experimental platform was constructed as shown in Figure 6(a). The proximal end of the ESBA was clamped to an aluminum frame in the vertical direction to reduce the influence of gravity. A 3D Guidance trakSTAR (Ascension Corp., USA) was chosen to measure the position by attaching a probe on the end with accuracy up to 0.1mm. A high-definition camera (Eos 6D, Canon Inc., Japan) was also used to capture the deformation of ESBAs from the side view, and then the bending angles of photos were measured on the computer by the commercial CAD software AutoCAD (Autodesk Inc.). We used to tension and compression tester (ZQ-21B, Zhiqu Corp., China) to provide an external payload in the horizontal direction. The air inlet was connected with a proportional valve (IVT2000, SMC Corp., Japan) to control the input air pressure by varying the analog voltage. Here, we also present one of the test results under the same conditions as given in Figure 5 for the FEM simulation. The bending angle is 251.8° as is shown in Figure 6(b).
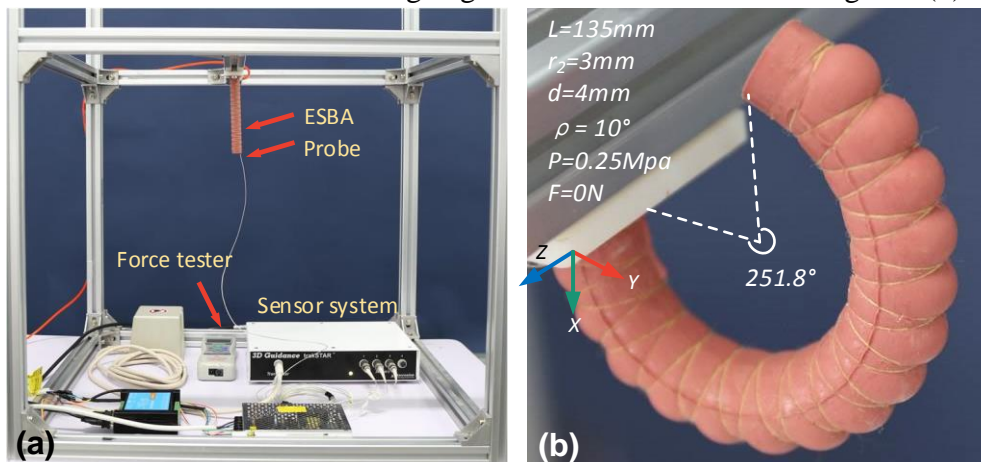

Figure 6. The experimental platform and a test result

4.4 Validation

To validate the analytical model there is a question about how many segments are required to ensure a good approximation of the deformation without unnecessary computational cost. Additionally, under different loading conditions, the proper number of the segment will also change. In the unloaded case, the bending deformation of the ESBA is of constant radius of curvature, so only one segment is required. However, when external forces are applied the bending deformation of the ESBA will exhibit the non-constant radius of curvature, so it needs multiple segments. Generally, with the growth of the number of segments n, the resolution of the analytical model will increase at the expense of computational time. How to determine a proper number of segments in a specific condition will be analyzed in Section 4.4.2.

4.4.1 Bending without payload

Using the design parameters in Table 1, we use an input pressure of 0.2MPa without an external payload to obtain the bending angles by an analytical model, FEM model and experiments as presented in Figure 7(a). The results of these three methods are 179.5°, 183.1°, and 176.8°, respectively, with resulting errors of the analytical model and FEM model, are 2.7° and 6.3° but both under 5% of the total experimental displacement. We then increased the pressure from 0-0.2MPa to get more comprehensive results presented in Figure 7(b) where we found that the bending angle increases faster as the pressure is greater. Other angles of winding fibers at 5°, 15°, and 20° were also tested as shown in Figure 7b. It was found in these tests that the larger fiber angle results in a smaller bending output of the ESBA with the same air pressure due to greater component force in the axial direction of the ESBA.
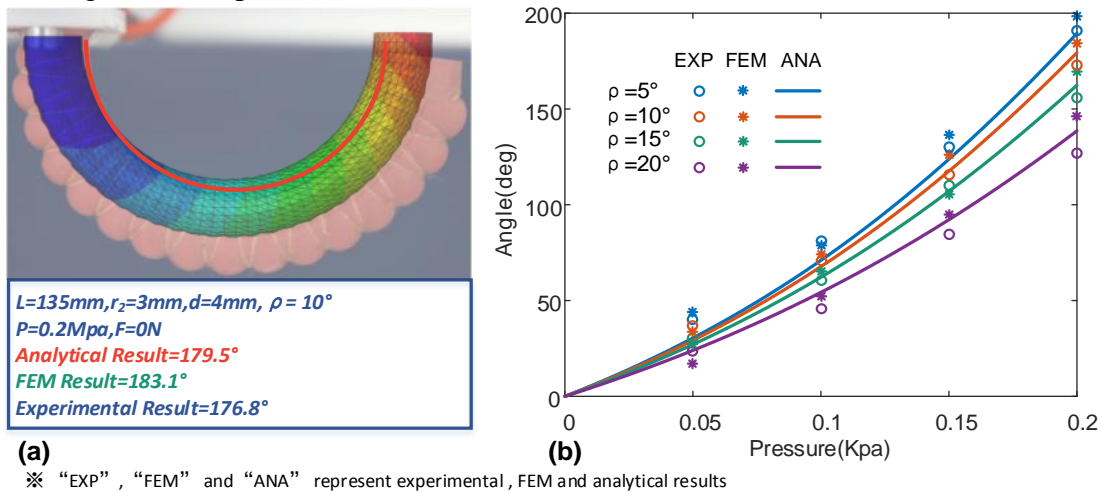

(a)

(b)

※ "EXP", "FEM" and "ANA" represent experimental, FEM and analytical results

Figure 7. Input pressure against bending angle results[※]

4.4.2 Bending under the payload

To achieve the desired bend angle of 90° using the parameters given in Table 1 the analytical and FEM models predict a required pressure of 0.123MPa and 0.121MPa respectively. Experimentally, it was found that a pressure of 0.124MPa was required. First, we applied a payload at the end in the horizontal direction from 0-2N gradually. In this condition, multiple segments are required to approximate the deformation of the ESBA prototype with a non-constant radius of curvature. Therefore, we continued to increase the number of segments in the analytical model until the gap is small enough to accept, which is obtained by comparing the results of the n segment and $n+1$ segment.

By increasing the number of segments, the end position and the bending angle of the ESBA under a payload of 1N and 2N in the horizontal direction are calculated by the analytical model, and the results of FEM and experiment are shown in Figure 8.
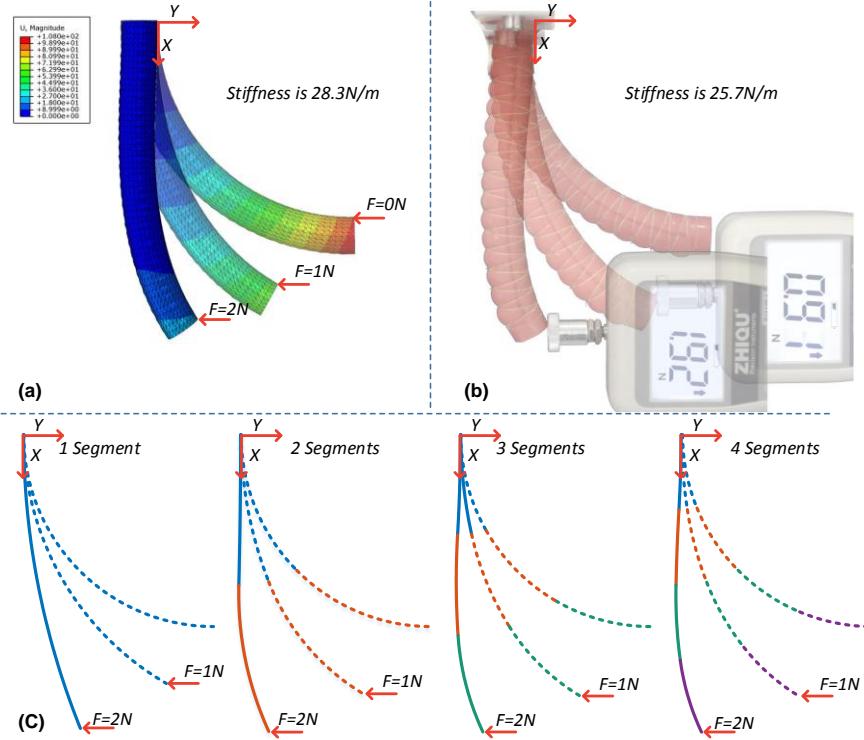

Figure 8. The shape of ESBA under the horizontal external payload: (a) the FEM results, (b) the experimental results and (c) analytical results

We found that the greater the number of segments used in the analytical model, the higher the resolution of the resulting deformation especially when the non-constant radius of curvature occurs. Additionally, the numerical results under 2N payload in the horizontal direction are shown in Table 2, where θ_{EXP}, θ_{FEM} present the bending angle obtained from the experiment and FEM simulation, respectively. For the analytical results, $\boldsymbol{\theta}=[\theta_1;\theta_2;\theta_3;\ldots,\theta_n]$ shows the bending angle of each segment. $e_\theta=\theta_{\text{TOL}}-\theta_{\text{EXP}}$ or $e_\theta=\theta_{\text{TOL}}-\theta_{\text{FEM}}$ is the bending angle error of the whole EBSA for the analytical model or FEM simulation against the prototype. The coordinate (x, y) presents the position of ESBA in S frame at the endpoint Q and e_{xy} is the distance of the FEM or analytical results compared with the experimental data.

Table 2 Results of ESBA under the 2N payload in the horizontal direction

Results	EXP	FEM	n=1	n=2	n=3	n=4
θ_{EXP} / θ_{FEM} / $\boldsymbol{\theta}$ (deg)	28.8	32.4	(22.1)	(-1.4, 26.2)	(-3.3, 7.1, 21.4)	(-3.3, 2.1, 9.0, 17.6)
θ_{TOL}	28.8	32.4	22.1	24.8	25.2	25.4
e_θ (deg)	N/A	3.6	-6.7	-4.0	-3.6	-3.4
x (mm)	133.5	125.6	131.6	133.0	133.2	133.3
y (mm)	8.1	15.3	25.7	12.7	10.2	9.2
e_{xy} (mm)	N/A	10.7	17.7	4.6	2.1	1.1

In Table 2, the error of the total bending angle e_θ decreases from -6.7° to -3.4° and the error of the end position e_{xy} decreases from 17.6mm to 1.1mm with the number of segments increasing. As mentioned above, the criteria for deciding how many segments to participate in the calculation is whether the two results of n segments and $n+1$ segments are close enough. Note the gaps between the three segments and four

segments for the bending angle and end position are 0.2 ° and 1.0mm, respectively. Though the deformation described by four segments has a higher resolution, we think the three-segment analytical model is enough for analyzing the case that the ESBA bends with or without payload.

We then applied a payload at the end in the vertical direction from 0-2N gradually. The end position and the bending angle of the ESBA under the payload of 1N and 2N in the vertical direction are shown in Figure 9. Similarly, we found that the bending angle of ESBA decreases when the external payload increases in the vertical direction. The numerical results under 2N payload in the vertical direction are shown in Table 3, where the bending angle errors for the analytic model and FEM model are -1.5 °and -3.0 °, respectively. In addition, the position errors for the analytic model and FEM model are 2.4mm and 4.9mm, respectively. These results prove that the proposed model can describe the deformation caused by a payload in any direction in the sagittal plane. For example, if an external payload acts on a point between the base and endpoint of the actuator, it can be considered that the proximal part from the base to the acting point is affected by the payload while the rest part from the acting point to the endpoint will bend without payload.
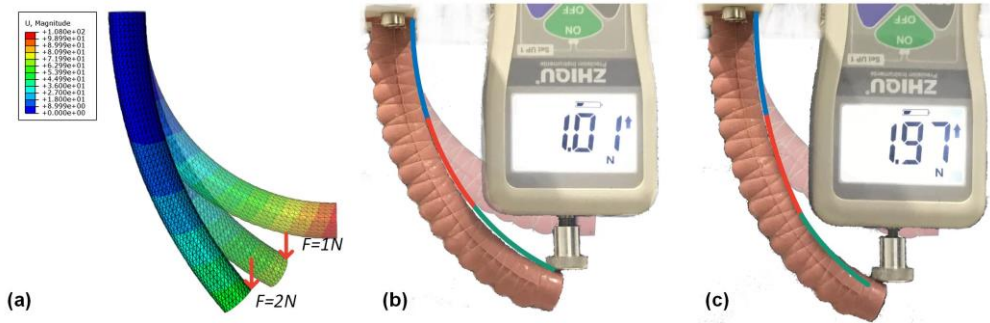

Figure 9. The shape of ESBA under the vertical external payload: (a) the FEM results, (b) the comparison with 1N and (c) the comparison with 2N

Table 3 Results of ESBA under the 2N payload in the vertical direction

Results	EXP	FEM	ANA
θ_{EXP} / θ_{FEM} / $\boldsymbol{\theta}$ (deg)	28.8	32.4	(12.4, 15.7, 23.6)
θ_{TOL}	53.2	50.2	51.7
e_{θ} (deg)	N/A	-3.0	-1.5
x (mm)	119.2	122.6	120.9
y (mm)	50.8	47.3	49.1
e_{xy} (mm)	N/A	4.9	2.4

4.4.3 Stiffness

In this section, we focus on the mechanical performances of the ESBA with regards to stiffness. Conventionally, the output force of the soft actuators is the only standard to evaluate their mechanical characteristics. To measure this, the endpoint of the soft actuator was kept still and the blocked-force measured by a force sensor while increasing the air pressure as reported in [23, 40]. However, this is not suitable, because soft actuators are usually accompanied by large nonlinear displacements when under external forces.

Taking the stiffness in the horizontal direction as the example, we started at a bending angle of 90 °, and then applied a payload tangentially to the tip of the actuator as shown in Figure 8(b). The relationship between the payload and the corresponding position of

the endpoint Q is shown in Figure 10, where the line, stars, and cycles are the results of the analytical model, FEM model, and experiments, respectively. It was found that the slope of the curve in the graph is not constant. Therefore, stiffness is defined as the ratio of the change of force to the resulting displacement $K=\Delta F/\Delta y$, where ΔF and Δy are the changes of force and displacement, respectively, with respect to the initial conditions (bending angle of 90 °, zero payload).
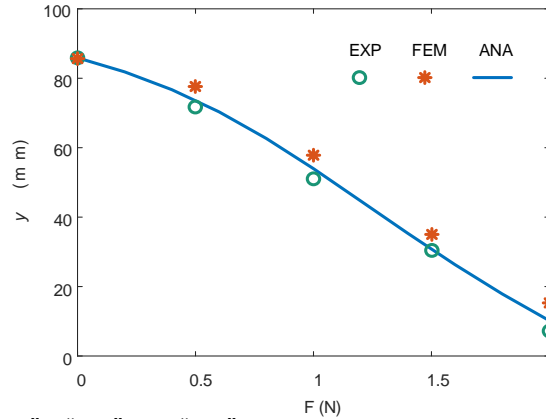
※ "EXP", "FEM" and "ANA" represent experimental, FEM and analytical results

Figure 10. The relationship between the payload and the position of endpoint[※]

For example, starting from the initial conditions, when the payload increases from 0N to 0.5N, the stiffness calculated by the analytical model, FEM model and experiment is 40.6N/m, 43.5N/m and 39.3 N/m, respectively. However, if the payload increases to 1N, the results become 31.2N/m, 33.7N/m and 29.1N/m, respectively. Then by applying a payload of 2N, the results are 26.4N/m, 28.3N/m, and 25.7N/m, respectively as shown in Figure 11. We found that even under the same initial condition, the increase of payload will result in reduction in stiffness.
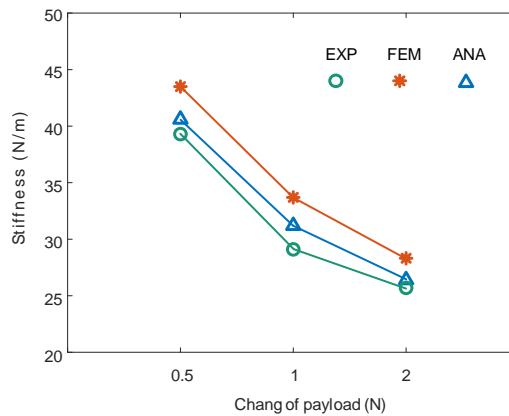
※ "EXP", "FEM" and "ANA" represent experimental, FEM and analytical results

Figure 11. The stiffness change with respect to different payloads[※]

4.4.4 Parameter Sweeps
In this section, we will reveal how geometric parameters affect the bending angle as well as the stiffness in the horizontal direction. For the bending angle without payload, we demonstrate the analytical results of the bending angle changing with two single variables, the radius of the chamber r_2 and the eccentric distance d, respectively but with the same fiber winding angle $\rho=10°$ and input air pressure $P = 0.2$Mpa, as shown in Figure 11. Different sets of orthogonal FEM simulation and experiment were also carried out using $r_2=2,4,6$ and $d =0,2,4,6$ under the same conditions. In Figure 12(a), for the same eccentric distance, the bending angles tend to increase with the increase of

r_2, especially close to the outer radius of the ESBA (r_1=8mm). This is because the radius of the chamber will have a squared effect on the cross-sectional moment generated by the pressure. Meanwhile, we also found that increasing r_2, rather than d, has a more pronounced effect on the bending angle, as shown in Figure 12(b).
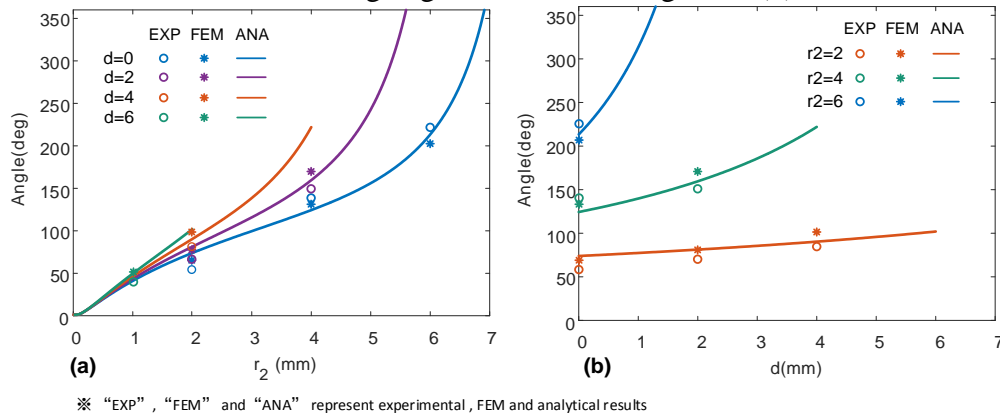

※ "EXP", "FEM" and "ANA" represent experimental, FEM and analytical results

Figure 12. Geometric parameters of ESBA against bending angle results

The analytical model was then utilized to carry out a full analysis of the impact of the design parameters on the bending angle. The possible geometric parameters, $r_2 \in (0,8)$, $d \in (0,8)$, $r_2+d<8$, are taken into account because of the geometric constraints. The bending angles are shown in Figure 13(a) under the same input air pressure 0.2Mpa. The conclusion can be drawn that the bending angle is significantly increased by upgrading the radius of chamber r_2.

For the analysis of the stiffness, in the following text, the stiffness is referring to the value calculated in the range of 0N to 2N similar to Section 4.4.3. The possible geometric parameters are the same as the above analysis. It is noted that, in order to ensure all the ESBAs' initial angle is 90°, the input air pressure is changeable according to its design parameters. This means that before calculating the stiffness, we need to find the air pressure that makes each ESBA just bend to 90° and then apply the payload. The stiffness with the geometric parameters changed is shown in Figure 13(b) by the 3D surface.
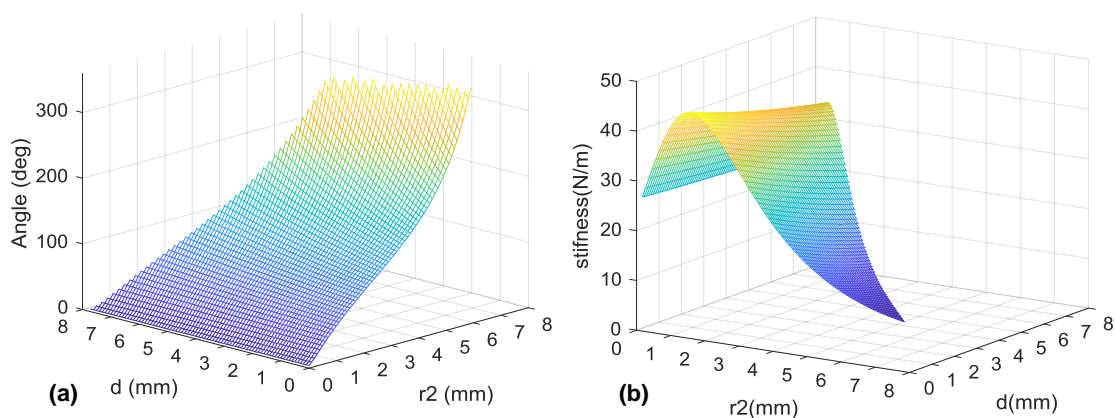

Figure 13. The performance of ESBA against geometric parameters

However, regarding the stiffness, the surface in Figure 13(b) does not have monotonicity. Instead, the general trend is that the smaller eccentric distance, d, and radius of the chamber, r_2, the greater stiffness the ESBAs have because they need more

pressure to bend to 90°, which leads to a larger moment. Nevertheless, when the radius is small enough, the area of pressure will quickly decrease, leading to a small moment.

5. Optimal design of ESBA

Through the above analysis, the relationship obtained by enumeration is tedious. Moreover, we still do not know what the exact best values of the design parameters are. Therefore, in this paper, the Particle Swarm Optimization (PSO) is introduced to find the best solutions containing radius of the chamber r_2 and the eccentric distance d to find the maximal stiffness with the same condition as mentioned in Section 4.4.3 [51, 52]. Based on the experience of the literature and the complexity of the proposed model, we firstly initialize a population of particle PN=30 and give the random positions and velocities on two dimensions in problem space. As in our case, the outer radius of the ESBA r_1 is limited to 8mm, the radius of chamber r_2 and eccentric distance d are also limited to a range from 0 mm to 8mm and the sum of these two variables must be less than 8 mm.

The fitness function was the formula for calculating the stiffness. The best position of particles was defined as the maximal stiffness and the optimization process are shown in Figure 14, where each circle represents a solution within the two-dimensional space and different colors indicate the different iterations. In the beginning, all of the particles are randomly scattered in the possible positions. After about 10 iterations, the solution with maximum stiffness has been found. After 50 iterations, all particles are concentrated near the optimal solution that is d=0, r_2=1.5305, and the maximal stiffness is 45.2974 N/m, which is consistent with the trend of analysis in Section 4.4.4 by parameter sweeps. The maximum bending angle and the maximum stiffness appear in the place where the eccentric distance d is zero. This is because the initial condition to evaluate the stiffness is firstly set by regulating the input air pressure to make ESBA bend to an initial angle of 90°. Then, the external payload is applied to identify the stiffness. In this way, different input air pressure is required to keep the initial bending angle constant while d and r_2 are changed. However, the different input air pressure itself also affects the stiffness of the actuator. Therefore, the optimization process eventually converges on to relatively small values of d and r_2, but implicates a high value of the input air pressure, to achieve maximum stiffness.
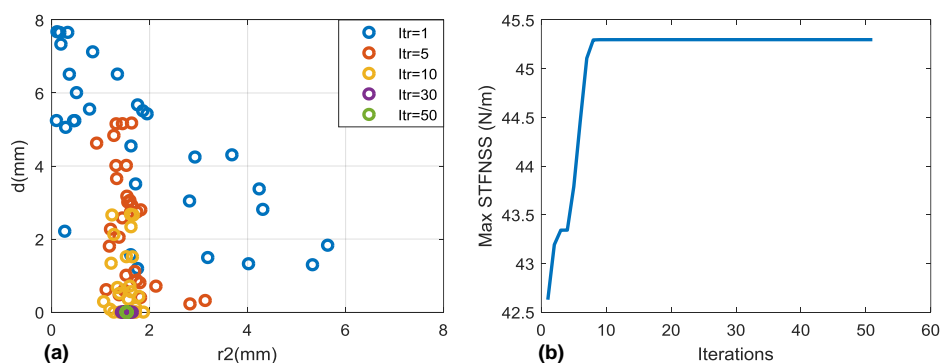

Figure 14. The process of PSO to find maximal stiffness

A new prototype is fabricated with the optimized parameters to validate if the proposed strategy is effective. In this case, the input air pressure of 0.2317Mpa is assigned so that the ESBA can bend to 90° without being subjected to external payloads in the initial state. The comparison results are shown in Figure 15, where the deformation obtained by the analytical model is basically consistent with the experimental results with the maximum error of bending angle and position are -3.0°

and 4.9mm, respectively. The experimental stiffness with 2N payload in the horizontal direction is calculated as 46.6200 N/m, which is also close to the optimized results 45.2974 N/m. In this way, we found the best design parameters and get rid of the 'trial and error' methods utilized in previous works.
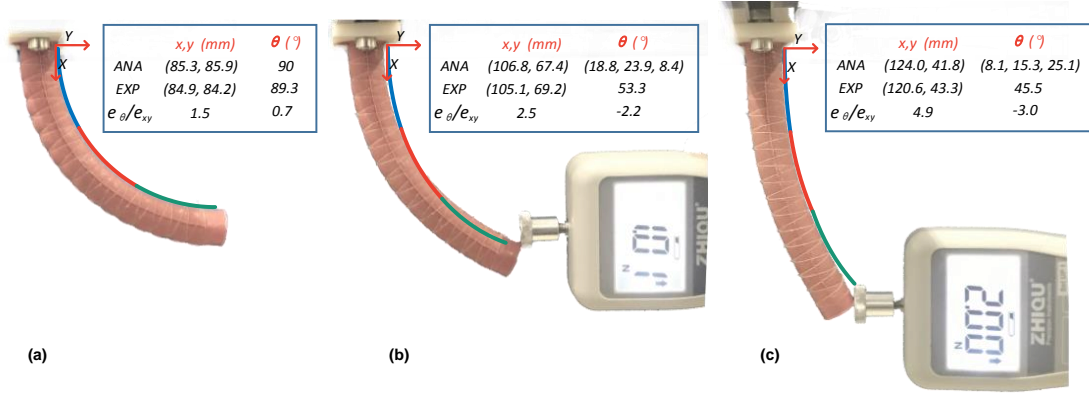

Figure 15. The validation with the optimized parameters

6. Conclusion

Soft actuators have various output characteristics such as nonlinear deformation, passive flexibility, and coupling of force-displacement, which is hard to describe when interacting with environments. In this paper, we proposed a concept of ESBAs that is a common situation for fiber-reinforcement soft bending actuators but can provide more combinations of design parameters to adapt to different required performances.

To obtain a kinematic-static coupling model, we solved the kinematics by introducing the screw theory based POE formula for its concise mathematical expression. The statics includes the effects of the input pressure, external payloads and design parameters on ESBAs. Through the presented model, FEM model and experiments, we found how the parameters affect the bending angle as well as the stiffness that is:

a)   If the maximum bending angle is the design target, the radius of the chamber, rather than the eccentric distance, should be preferentially increased under the same other conditions.

b)   If the maximum stiffness is the design target, there is no monotonous relationship between the design parameters and the outputs, and an optimization algorithm is required.

Therefore, this paper provides a relatively comprehensive analytic model of ESBA, which can be used for the optimization based design. The generalized model also helps to better understand the characteristics of conventional cylindrical fiber-reinforced soft actuators. In addition, it paves a way for the future investigation on more complicated applications such as the 3-D deformation under payloads acting on any position along the actuator length.

Appendix:

a.   In the framework of screw theory, the vector ξ_n called twist which has the form

$$\xi_n = \begin{bmatrix} -\omega_n \times q_n \\ \omega_n \end{bmatrix},$$

where $\omega_n \in \mathbb{R}^3$ is a unit vector in the direction of the twist axis and $q_n \in \mathbb{R}^3$ is any point on the axis. The vector ξ_n can be converted into homogeneous coordinate of 4×4 matrix $\hat{\xi}_n$ by the hat operator.

$$\hat{\xi}_n = \begin{bmatrix} \hat{\omega}_n & -\omega_n \times q_n \\ 0 & 0 \end{bmatrix}$$

where $\hat{\omega}_n = \begin{bmatrix} 0 & -\omega_{n1} & \omega_{n2} \\ \omega_{n3} & 0 & -\omega_{n1} \\ -\omega_{n2} & \omega_{n1} & 0 \end{bmatrix}$, $\omega_n = \begin{bmatrix} \omega_{n1} \\ \omega_{n2} \\ \omega_{n3} \end{bmatrix}$.

b. In Figure 3, the height of the shaded rectangle is $\left| d\left(r_1 \cos\alpha \right) \right| = r_1 \sin\alpha\, d\alpha$ and the width is $2r_1 \sin\alpha\, d\alpha$. Therefore, the area of the shaded region is $dS_{\mathrm{sld}} = 2r_1^2 \sin^2\alpha\, d\alpha$, which is also the small element of the circular area.

References

[1] Laschi, C., Mazzolai, B., and Cianchetti, M., 2016, "Soft Robotics: Technologies and Systems Pushing the Boundaries of Robot Abilities," Science Robotics, **1**(1), p. eaah3690. DOI:10.1126/scirobotics.aah3690

[2] Bao, G., Fang, H., Chen, L., Wan, Y., Xu, F., Yang, Q., and Zhang, L., 2018, "Soft Robotics: Academic Insights and Perspectives Through Bibliometric Analysis," Soft Robotics, **5**(3), pp. 229-241. DOI:10.1089/soro.2017.0135

[3] Rus, D., and Tolley, M. T., 2015, "Design, Fabrication and Control of Soft Robots," Nature, **521**(7553), pp. 467-475. DOI:10.1038/nature14543

[4] Seok, S., Onal, C. D., Cho, K., Wood, R. J., Rus, D., and Kim, S., 2013, "Meshworm: a Peristaltic Soft Robot with Antagonistic Nickel Titanium Coil Actuators," IEEE/ASME Transactions on Mechatronics, **18**(5), pp. 1485-1497. DOI:10.1109/tmech.2012.2204070

[5] Chen, Z., Shatara, S., and Tan, X., 2010, "Modeling of Biomimetic Robotic Fish Propelled by an Ionic Polymer–Metal Composite Caudal Fin," IEEE/ASME Transactions on Mechatronics, **15**(3), pp. 448-459. DOI:10.1109/tmech.2009.2027812

[6] Jung, K., Koo, J. C., Lee, Y. K., and Choi, H. R., 2007, "Artificial Annelid Robot Driven by Soft Actuators," Bioinspiration & Biomimetics, **2**(2), p. S42. DOI:10.1088/1748-3182/2/2/S05

[7] Li, H., Go, G., Ko, S. Y., Park, J.-O., and Park, S., 2016, "Magnetic Actuated PH-Responsive Hydrogel-Based Soft Micro-Robot for Targeted Drug Delivery," Smart Materials and Structures, **25**(2), p. 027001. DOI:10.1088/0964-1726/25/2/027001

[8] Salerno, M., Zhang, K., Menciassi, A., and Dai, J. S., 2016, "A Novel 4-DOF Origami Grasper With an SMA-Actuation System for Minimally Invasive Surgery," IEEE Transactions on Robotics, **32**(3), pp. 484-498. DOI:10.1109/TRO.2016.2539373

[9] Kang, R., Guo, Y., Chen, L., Branson, D., and Dai, J. S., 2016, "Design of a Pneumatic Muscle Based Continuum Robot with Embedded Tendons," IEEE/ASME Transactions on Mechatronics, **22**(2), pp. 751-761. DOI:10.1109/tmech.2016.2636199

[10] Doumit, M., Fahim, A., and Munro, M., 2009, "Analytical Modeling and Experimental Validation of the Braided Pneumatic Muscle," IEEE Transactions on Robotics, **25**(6), pp. 1282-1291. DOI:10.1109/tro.2009.2032959

[11] Cao, K., Kang, R., Branson, D. T., Geng, S., Song, Z., and Dai, J. S., 2017, "Workspace Analysis of Tendon-Driven Continuum Robots Based on Mechanical Interference Identification," Journal of Mechanical Design, **139**(6), p. 062303. DOI:10.1115/1.4036395

[12] Ilievski, F., Mazzeo, A. D., Shepherd, R. E., Chen, X., and Whitesides, G. M., 2011, "Soft Robotics for Chemists," Angewandte Chemie-International Edition, **50**(8), pp. 1890-1895. DOI:10.1002/anie.201006464

[13] Mosadegh, B., Polygerinos, P., Keplinger, C., Wennstedt, S., Shepherd, R. F., Gupta, U., Shim, J., Bertoldi, K., Walsh, C. J., and Whitesides, G. M., 2014, "Pneumatic Networks for Soft Robotics that Actuate Rapidly," Advanced Functional Materials, **24**(15), pp. 2163-2170. DOI:10.1002/adfm.201303288

[14] Elsayed, Y., Vincensi, A., Lekakou, C., Geng, T., Saaj, C., Ranzani, T., Cianchetti, M., and Menciassi, A., 2014, "Finite Element Analysis and Design Optimization of a Pneumatically Actuating Silicone Module for Robotic Surgery Applications," Soft Robotics, **1**(4), pp. 255-262. DOI:10.1089/soro.2014.0016

[15] Mac Murray, B. C., An, X., Robinson, S. S., van Meerbeek, I. M., O'Brien, K. W., Zhao, H., and Shepherd, R. F., 2015, "Poroelastic Foams for Simple Fabrication of Complex Soft Robots," Advanced Materials, **27**(41), pp. 6334-6340. DOI:10.1002/adma.201503464

[16] Robertson, M. A., and Paik, J., 2017, "New Soft Robots Really Suck: Vacuum-Powered Systems Empower Diverse Capabilities," Science Robotics, **2**(9), p. eaan6357. DOI:10.1126/scirobotics.aan6357

[17] Galloway, K. C., Polygerinos, P., Walsh, C. J., and Wood, R. J., 2013, "Mechanically Programmable Bend Radius for Fiber-Reinforced Soft Actuators," 2013 International Conference on Advanced Robotics (ICAR). DOI:10.1109/icar.2013.6766586

[18] McMahan, W., Chitrakaran, V., Csencsits, M., Dawson, D., Walker, I. D., Jones, B. A., Pritts, M., Dienno, D., Grissom, M., and Rahn, C. D., 2006, "Field Trials and Testing of the Octarm Continuum Manipulator," 2006 IEEE International

Conference on Robotics and Automation (ICRA), **1-10**. DOI:10.1109/robot.2006.1642051

[19] Kang, R., Branson, D. T., Zheng, T., Guglielmino, E., and Caldwell, D. G., 2013, "Design, modeling and control of a pneumatically actuated manipulator inspired by biological continuum structures," Bioinspiration & Biomimetics, **8**(3), p. 036008. DOI:10.1088/1748-3182/8/3/036008

[20] Kim, S., Laschi, C., and Trimmer, B., 2013, "Soft Robotics: A Bioinspired Evolution in Robotics," Trends in Biotechnology, **31**(5), pp. 23-30. DOI:10.1016/j.tibtech.2013.03.002

[21] Sun, Y., Song, Y. S., and Paik, J., 2013, "Characterization of Silicone Rubber Based Soft Pneumatic Actuators," 2013 IEEE International Conference on Intelligent Robots and Systems (IROS), pp. 4446-4453. DOI:10.1109/iros.2013.6696995

[22] Kothera, C. S., Jangid, M., Sirohi, J., and Wereley, N. M., 2009, "Experimental characterization and static modeling of McKibben actuators," Journal of Mechanical Design, **131**(9), p. 091010. DOI:10.1115/1.3158982

[23] Moseley, P., Florez, J. M., Sonar, H. A., Agarwal, G., Curtin, W., and Paik, J., 2016, "Modeling, Design, and Development of Soft Pneumatic Actuators with Finite Element Method," Advanced Engineering Materials, **18**(6), pp. 978-988. DOI:10.1002/adem.201500503

[24] Howell, L. L., and Midha, A., 1995, "Parametric Deflection Approximations for End-Loaded, Large-Deflection Beams in Compliant Mechanisms," Journal of Mechanical Design, **117**(1), pp. 156-165. DOI:10.1115/1.2826101

[25] Satheeshbabu, S., and Krishnan, G., 2019, "Modeling the Bending Behavior of Fiber-Reinforced Pneumatic Actuators Using a Pseudo-Rigid-Body Model," Journal of Mechanisms and Robotics, **11**(3), pp. 031011-031011-031019. DOI:10.1115/1.4042632

[26] Venkiteswaran, V. K., and Su, H.-J., 2016, "A Three-Spring Pseudorigid-Body Model for Soft Joints With Significant Elongation Effects," Journal of Mechanisms and Robotics, **8**(6), pp. 061001-061001-061007. DOI:10.1115/1.4032862

[27] Webster, R. J., and Jones, B. A., 2010, "Design and Kinematic Modeling of Constant Curvature Continuum Robots: A Review," International Journal of Robotics Research, **29**(13), pp. 1661-1683. DOI:10.1177/0278364910368147

[28] Xu, K., and Simaan, N., 2009, "Analytic Formulation for Kinematics, Statics, and Shape Restoration of Multibackbone Continuum Robots Via Elliptic Integrals," Journal of Mechanisms and Robotics, **2**(1), p. 011006. DOI:10.1115/1.4000519

[29] Mahl, T., Hildebrandt, A., and Sawodny, O., 2014, "A variable curvature continuum kinematics for kinematic control of the bionic handling assistant," IEEE Transactions on Robotics, **30**(4), pp. 935-949. DOI:10.1109/tro.2014.2314777

[30] Dai, J. S., 2006, "An historical review of the theoretical development of rigid body displacements from Rodrigues parameters to the finite twist," Mechanism and Machine Theory, **41**(1), pp. 41-52. DOI:10.1016/j.mechmachtheory.2005.04.004

[31] Selig, J. M., and Ding, X., 2009, "A Screw Theory of Timoshenko Beams," Journal of Applied Mechanics, **76**(3), pp. 031003-031003-031007. DOI:10.1115/1.3063630

[32] Ding, X., and Dai, J. S., 2010, "Compliance Analysis of Mechanisms with Spatial Continuous Compliance in the Context of Screw Theory and Lie Groups," Proceedings of the Institution of Mechanical Engineers, Part C: Journal of Mechanical Engineering Science, **224**(11), pp. 2493-2504. DOI:10.1243/09544062jmes2095

[33] Qi, P., Qiu, C., Liu, H., Dai, J. S., Seneviratne, L. D., and Althoefer, K., 2016, "A Novel Continuum Manipulator Design Using Serially Connected Double-Layer Planar Springs," IEEE/ASME Transactions on Mechatronics, **21**(3), pp. 1281-1292. DOI:10.1109/TMECH.2015.2498738

[34] He, B., Xu, S., and Wang, Z., 2018, "Research on Stiffness of Multibackbone Continuum Robot Based on Screw Theory and Euler-Bernoulli Beam," Mathematical Problems in Engineering, **2018**, pp. 1-16. DOI:10.1155/2018/6910468

[35] Gao, G., Hao, W., Xia, Q., Song, M., and Han, R., 2016, "Study on the load capacity of a single-section continuum manipulator," Mechanism and Machine Theory, **104**, pp. 313-326. DOI:10.1016/j.mechmachtheory.2016.06.010

[36] Rucker, D. C., and Webster, R. J., 2011, "Statics and Dynamics of Continuum Robots With General Tendon Routing and External Loading," IEEE Transactions on Robotics, **27**(6), pp. 1033-1044. DOI:10.1109/tro.2011.2160469

[37] Rone, W. S., and Ben-Tzvi, P., 2014, "Continuum Robot Dynamics Utilizing the Principle of Virtual Power," IEEE Transactions on Robotics, **30**(1), pp. 275-287. DOI:10.1109/tro.2013.2281564

[38] Trivedi, D., Lotfi, A., and Rahn, C. D., 2008, "Geometrically exact models for soft robotic manipulators," IEEE Transactions on Robotics, **24**(4), pp. 773-780. DOI:10.1109/tro.2008.924923

[39] Bishop-Moser, J., and Kota, S., 2015, "Design and modeling of generalized fiber-reinforced pneumatic soft actuators," IEEE Transactions on Robotics, **31**(3), pp. 536-545. DOI:10.1109/tro.2015.2409452

[40] Polygerinos, P., Wang, Z., Overvelde, J. T. B., Galloway, K. C., Wood, R. J., Bertoldi, K., and Walsh, C. J., 2015, "Modeling of Soft Fiber-Reinforced Bending Actuators," IEEE Transactions on Robotics, **31**(3), pp. 778-789. DOI:10.1109/tro.2015.2428504

[41] Trivedi, D., Dienno, D., and Rahn, C. D., 2008, "Optimal, model-based design of soft robotic manipulators," Journal of Mechanical Design, **130**(9), p. 091402. DOI:10.1115/1.2943300

[42] Connolly, F., Walsh, C. J., and Bertoldi, K., 2017, "Automatic Design of Fiber-Reinforced Soft Actuators for Trajectory Matching," Proceedings of the National Academy of Sciences of the United States of America, **114**(1), pp. 51-56. DOI:10.1073/pnas.1615140114

[43] Brockett, R. W., "Robotic manipulators and the product of exponentials formula," Proc. Mathematical theory of networks and systems, Springer, pp. 120-129. DOI:10.1007/BFb0031048

[44] Murray, R. M., Sastry, S. S., and Li, Z., 1994, A Mathematical Introduction to Robotic Manipulation, CRC Press, Inc.

[45] Dai, J. S., 2012, "Finite Displacement Screw Operators With Embedded Chasles' Motion," Journal of Mechanisms and Robotics, **4**(4), pp. 041002-041002-041009. DOI:10.1115/1.4006951

[46] Langhaar, H. L., 1962, Energy Methods in Applied Mechanics, Courier Dover Publications.

[47] Reddy, J. N., 1984, Energy Principles and Variational Methods in Applied Mechanics, John Wiley & Sons.

[48] Greaves, G. N., Greer, A. L., Lakes, R. S., and Rouxel, T., 2011, "Poisson's Ratio and Modern Materials," Nature Materials, **10**(11), pp. 823-837. DOI:10.1038/nmat3134

[49] Martins, P., Jorge, R., and Ferreira, A., 2006, "A Comparative Study of Several Material Models for Prediction of Hyperelastic Properties: Application to Silicone‐Rubber and Soft Tissues," Strain, **42**(3), pp. 135-147. DOI:10.1111/j.1475-1305.2006.00257.x

[50] Yang, D., Verma, M. S., So, J. H., Mosadegh, B., Keplinger, C., Lee, B., Khashai, F., Lossner, E., Suo, Z., and Whitesides, G. M., 2016, "Buckling Pneumatic Linear Actuators Inspired by Muscle," Advanced Materials Technologies, **1**(3). DOI:10.1002/admt.201600055

[51] Poli, R., Kennedy, J., and Blackwell, T., 2007, "Particle Swarm Optimization," Swarm Intelligence, **1**(1), pp. 33-57. DOI:10.1007/s11721-007-0002-0

[52] Kennedy, J., 2010, Particle Swarm Optimization, Springer US, Boston, MA. DOI:10.1007/978-0-387-30164-8_630